nature physics

Article

https://doi.org/10.1038/s41567-025-02839-3

Active membrane deformations of a minimal synthetic cell

Received: 22 November 2023

Accepted: 21 February 2025

Published online: 24 March 2025

Check for updates

Alfredo Sciortino[1,2,7], Hammad A. Faizi[3,7], Dmitry A. Fedosov[4,7], Layne Frechette[5], Petia M. Vlahovska[6], Gerhard Gompper[4] ✉ & Andreas R. Bausch[1,2] ✉

Living cells can adapt their shape in response to their environment, a process driven by the interaction between their flexible membrane and the activity of the underlying cytoskeleton. However, the precise physical mechanisms of this coupling remain unclear. Here we show how cytoskeletal forces acting on a biomimetic membrane affect its deformations. Using a minimal cell model that consists of an active network of microtubules and molecular motors encapsulated inside lipid vesicles, we observe large shape fluctuations and travelling membrane deformations. Quantitative analysis of membrane and microtubule dynamics demonstrates how active forces set the temporal scale of vesicle fluctuations, giving rise to fluctuation spectra that differ in both their spatial and temporal decays from their counterparts in thermal equilibrium. Using simulations, we extend the classical framework of membrane fluctuations to active cytoskeleton-driven vesicles, demonstrating how correlated activity governs membrane dynamics and the roles of confinement, membrane material properties and cytoskeletal forces. Our findings provide a quantitative foundation for understanding the shape-morphing abilities of living cells.

Rather than being merely passive containers, cell membranes actively respond to and steer cellular activity, enabling a myriad of biological functions such as cell crawling, cell division and cytoplasmic streaming[1–8]. Moreover, nucleus deformations can affect transcription[9], and prebiotic membrane deformations might have influenced the origin of life[10]. To accomplish these activities, cells have the ability to dramatically change their shape, and many of these processes arise from a tight coupling between lipid membrane fluctuations (providing the necessary flexibility) and the underlying cytoskeleton, which provides the necessary active forces and directionality to induce deformations. The seminal discovery of 'membrane flickering' in red blood cells[11,12] revealed how fluctuation analysis is essential to understand membrane-driven processes both in vivo[13–16] and in vitro[17–19]. One general result at equilibrium is that the temporal relaxation of membrane fluctuations is tightly bound to its spatial correlations[20–23], enabling the extraction of mechanical properties from both spatial and temporal measurements of membrane dynamics. However, in cells, cytoskeletal activity modifies both spatial and temporal behaviours of membrane deformations[13,14], potentially breaking their interdependence dictated by thermodynamics[23–27]. Hence, in living systems, it is challenging to simultaneously measure the dynamics of both membrane and cytoskeleton imparting forces on it and to draw a precise link between cytoskeletal activity and its resulting fluctuations.

Giant unilamellar vesicles (GUVs) are a powerful tool to investigate, in a controlled minimal system, how membrane deformations behave[17,19,22] and how they are affected by activity[28–35]. However, despite

[1]Lehrstuhl für Zellbiophysik (E27), Physik Department, Technische Universität München, Garching bei München, Germany. [2]Center for Protein Assemblies, Garching bei München, Germany. [3]Department of Mechanical Engineering, Northwestern University, Evanston, IL, USA. [4]Theoretical Physics of Living Matter, Institute for Advanced Simulation, Forschungszentrum Jülich, Jülich, Germany. [5]Martin A. Fisher School of Physics, Brandeis University, Waltham, MA, USA. [6]Department of Engineering Sciences and Applied Mathematics, Northwestern University, Evanston, IL, USA. [7]These authors contributed equally: Alfredo Sciortino, Hammad A. Faizi, Dmitry A. Fedosov. ✉e-mail: g.gompper@fz-juelich.de; abausch@mytum.de

https://doi.org/10.1038/s41567-025-02839-3

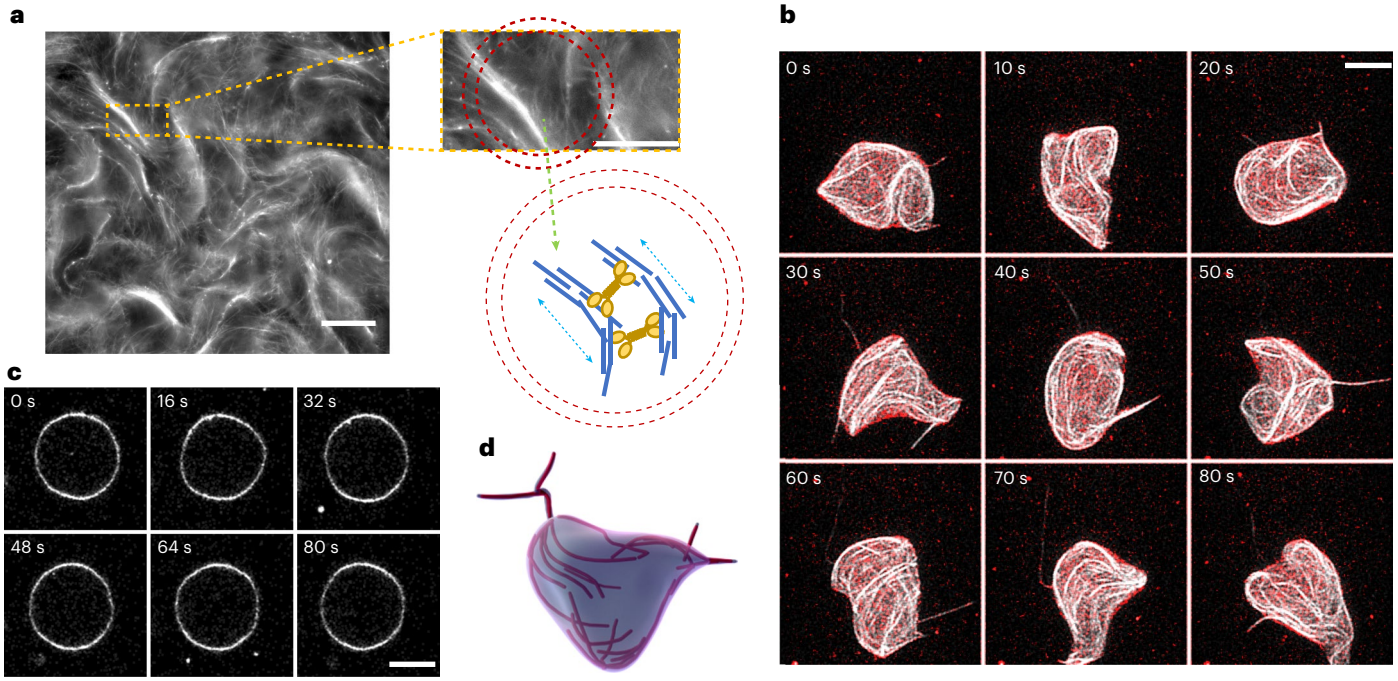

Fig. 1 | GUVs containing a minimal cytoskeleton exhibit large shape fluctuations. a, Confocal snapshot of the active MT network in unconfined conditions. Short fluorescently labelled MTs, in the presence of crosslinkers, self-organize into extensile active bundles, propelled by kinesin motors (right). Scale bar, 100 µm. This experiment was repeated twice. Top right: enlargement of the extensile bundles. A circle having a size comparable with the GUVs we produce ($R_0 \approx 25$ µm) is superimposed in red for reference. Scale bar, 50 µm. Bottom right: schematic of the encapsulated experimental system. Inside the GUV (red circle), small MTs of opposite polarities assemble into bundles that are extended (see arrows) by kinesin motors (in yellow). This results in active extensile bundles confined inside the GUV. **b**, Confocal projections of a GUV (membrane in red) containing an active MT network (MTs are shown in white). The GUV deforms and changes shape with a timescale of the order of several (~10) seconds. Scale bar, 20 µm. **c**, A passive vesicle fluctuating with the same time interval between frames as a reference. Scale bar, 20 µm. **d**, Artistic depiction of shape-morphing GUVs resulting from the encapsulation of active bundles.

progress[32,36–47], replicating cell-like shape deformations using a minimal system remains elusive. Here we address this issue by encapsulating a reconstituted cytoskeleton composed of an active microtubule (MT) network inside a deformable GUV, and analysing the resulting fluctuations and shape deformations.

Vesicle shapes induced by active bundles

Our experimental cytoskeleton model consists of an active gel of MTs and molecular motors, similar to previously reported systems[37,48–52], encapsulated inside GUVs using the continuous droplet interface crossing encapsulation (cDICE) technique[53,54]. Microscopically, the active system is composed of short (~1 µm), stabilized MTs (at concentration c_{MT}), kinesin tetramers (at concentration c_K) and a crosslinker. Here, instead of the usual choice of having a depletant (such as polyethylene glycol), as a crosslinker, we use the protein anillin (at concentration c_A), which induces filament–filament interactions leading to the formation of MT bundles (Supplementary Fig. 1a). Because of the additional activity of molecular motors acting on filaments, bundles extend and buckle due to kinesin-induced stresses (Fig. 1a), continuously breaking and aggregating, as long as adenosine triphosphate (ATP) is available (for 1 h, under our conditions). Using crosslinkers instead of depletants, and keeping the MT concentration in a dilute regime, we ensure that the bundles are not effectively attracted to the membrane (as they would in the presence of a depletion interaction) and are not dense enough to form a nematic material[55]. The net result is a minimal active cytoskeleton, which self-organizes into a loosely connected, isotropic three-dimensional network of long (~100 µm) extensile bundles. When encapsulated inside GUVs (mean radius, $R_0 \approx 25$ µm), this active MT network assembles inside the whole vesicle volume, in stark contrast to previous systems consisting of a dense two-dimensional nematic layer on the membrane[37]. Yet, when active bundles hit the membrane, the forces exerted by the MT gel induce large shape deformations of the vesicle (Fig. 1b and Supplementary Video 1). The GUV continuously undergoes dramatic morphological changes, with a timescale of ~10 s, as extracted by the correlation function of membrane deformations (Supplementary Fig. 5c). Active deformations are clearly different in magnitude and dynamics from those present at equilibrium (Fig. 1c). They are observed for a wide range of concentrations of MTs, kinesin and anillin (Supplementary Fig. 1b). These enhanced deformations are tightly correlated with the organization of the MT network inside the GUV (Fig. 1d and Supplementary Video 2). Since MTs do not assemble into a nematic layer, the deformations here are not localized to topological defects in the alignment of filaments[37] but are a direct result of bundles exerting local forces on the membrane by their kinesin-induced extension. Moreover, vesicles never settle into a definite shape as observed in previous systems[28,30,32], but rather continuously fluctuate around a spherical geometry.

Fluctuation spectroscopy reveals enhanced out-of-equilibrium fluctuations

More insights into the active membrane deformations can be gained by an analysis of the shape of the GUVs. First, we take long, high-frame-rate videos of the equatorial plane of a deforming GUV (30–4 frames per second; Supplementary Video 3) and extract its contour $R(\phi, t)$ (Fig. 2a). From this, we compute the distribution of membrane deformations $\Delta R = R - R_0$, where R_0 is the mean radius. Deformations are averaged over a variable duration τ_{avg}. We obtain large (~20%R_0) deformations with a non-Gaussian distribution, especially for short τ_{avg} (Fig. 2b), indicating that the temporal behaviour of the active vesicles is distinct from the equilibrium counterpart (Fig. 2c), which instead shows smaller, Gaussian deformations. The difference is further validated by

https://doi.org/10.1038/s41567-025-02839-3

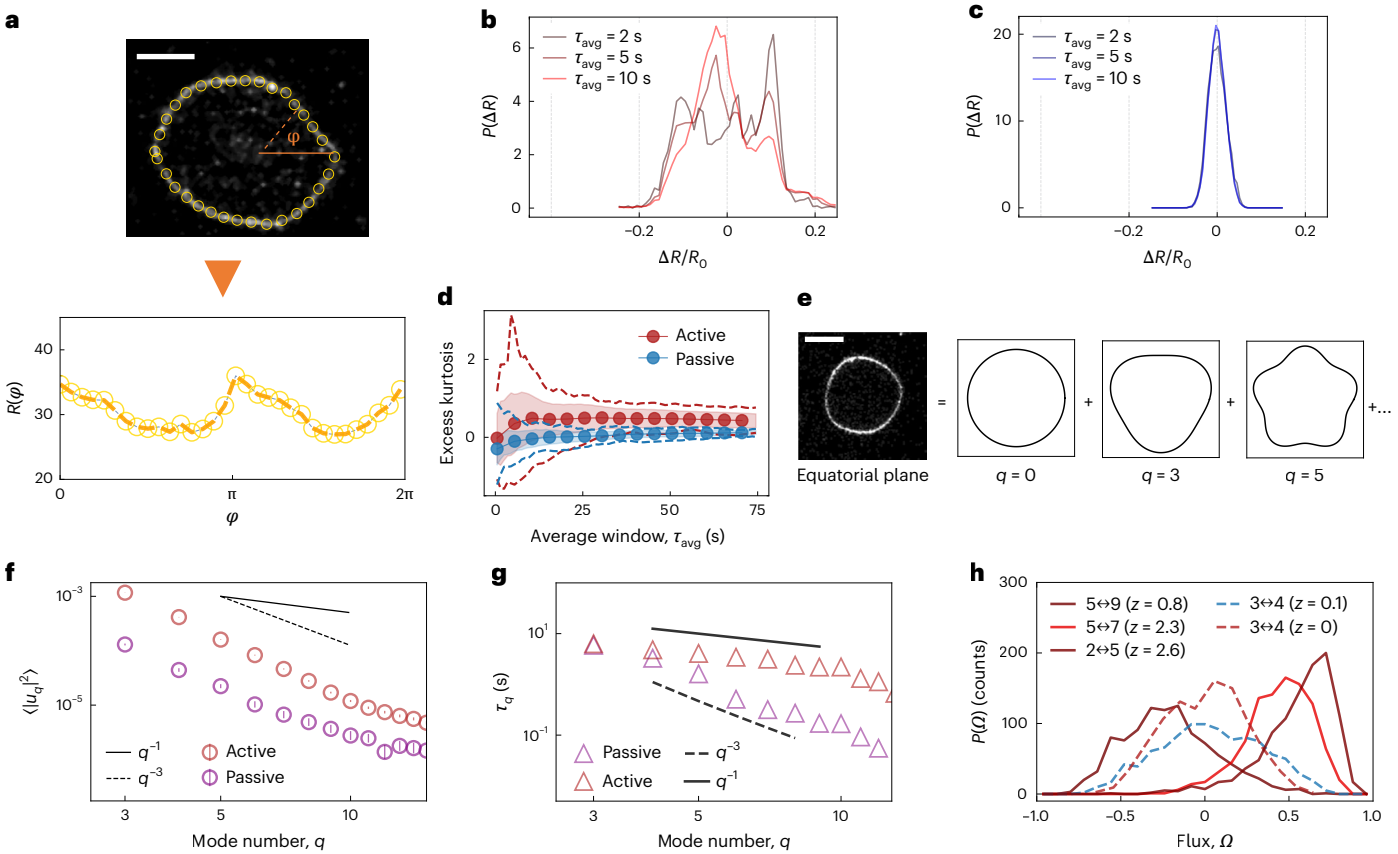

Fig. 2 | Membrane deformations of active vesicles are out of equilibrium. a, To analyse deformations, the equatorial contour of a fluctuating vesicle is tracked to obtain its description in polar coordinates $R(\phi, t)$. The extracted contour is marked by orange dots and then shown as a (ϕ, R) plot (bottom). The dashed line is a guide for the eye. Scale bar, 25 µm. **b**,**c**, Histograms of the distribution of radial deformations $P(\Delta R)$ for an active GUV (**b**), compared with a passive one (**c**), normalized by the mean radius R_0. The contours are sampled for different times (τ_{avg} = 2 s, 5 s and 10 s) from the videos of GUVs. Active deformations have peculiar distributions at short timescales, indicating correlated dynamics. Passive GUVs exhibit a Gaussian-like distribution at all timescales, as expected from thermal noise. **d**, Excess kurtosis of the distribution of radial deformations as a function of sampling time τ_{avg} for an active (red) and a passive (blue) GUV. The circles indicate the mean, the shaded area indicates the s.d. and the dashed lines indicate the minimum/maximum kurtosis. Data are generated by extracting frames from recordings of a given duration τ_{avg} and computing the kurtosis of the distribution of radial deformations. At a short timescale, the difference in spread between active and passive is noticeable. **e**, Schematic of the decomposition of the contour into a sum of Fourier modes, labelled with q, whose fluctuations can then be separately analysed. **f**, Fluctuation spectrum for the Fourier coefficients u_q as a function of Fourier mode q for a passive (purple) and an active (red) GUV. Fluctuations of the active GUV are higher in magnitude and decay with a scaling exponent of ~3. The dashed line indicates a q^{-3} scaling and the solid black line, a q^{-1} scaling. Data are shown as mean ± standard error of the mean, derived from the precision of the contour detection based on the optical resolution of the camera. The error bars are smaller than the symbols. **g**, Correlation time τ_q at each mode q for a passive (purple) and an active (red) vesicle, as obtained from the correlation functions $\langle u_q^*(t)u_q(0)\rangle$. Although the passive vesicle exhibits the expected q^{-3} scaling (dashed line), the active one has a different one (solid line indicates q^{-1}). **h**, Histogram of the flux between mode Ω showing broken detailed balance between pairs of different modes, a signature of the out-of-equilibrium activity. The dashed blue line shows an example from a passive vesicle showing no net flux. For each dataset, we compute the z score as the mean divided by the s.d. (Supplementary Section 2.4), indicating how far the mean is from $\Omega = 0$. One example in that even in the active case, there is no net flux (red dashed line).

an analysis of the distributions' kurtosis as τ_{avg} is varied, indicating that active GUVs at short times ($\tau_{avg} \approx 2$ s) show variations from a Gaussian distribution due to activity. At long averaging times instead ($\tau_{avg} \approx 10$ s), active deformations also approach bell-shaped distributions, although with a larger variance (Fig. 2d).

To gain further insights into the spatiotemporal dynamics of active GUVs, we resort to flicker spectroscopy. The contour is decomposed into Fourier modes, with mode number q (Fig. 2e and Supplementary Section 2) as

$$R(\phi, t) = R_0\left(1 + \sum_{q}^{q_{max}} u_q(t)e^{iq\phi}\right), \quad (1)$$

where $q_{max} \approx 15$ is fixed by the image resolution. Each coefficient u_q represents the magnitude of equatorial deformations of wavelength ~R/q.

For passive vesicles with bending rigidity κ and tension σ, the power spectrum of the Fourier coefficients u_q is expected to scale as

$$\langle |u_q|^2 \rangle \approx \frac{k_B T}{\kappa} \frac{1}{q^3 + \bar{\sigma} q}, \quad (2)$$

where $k_B T$ is the thermal energy and $\bar{\sigma} = \sigma R_0^2/\kappa$ is the normalized tension. Note that this equation for the equatorial fluctuations of a GUV is the equivalent of the classical Canham–Helfrich expression but for a quasi-spherical membrane on an equatorially intersecting plane[17,20,21]. For passive vesicles, we recover the classical regimes of bending ($\bar{\sigma} \ll 1$; Fig. 2f, purple) and tension-dominated fluctuations ($\bar{\sigma} \gg 1$; Supplementary Fig. 2a). From these data, for passive GUVs made of egg phosphatidylcholine, we extract the bending rigidity of $\kappa_{pass} = (13.4 \pm 2.5)\, k_B T$ (mean + s.d., $n = 5$). This value is consistent with those in the literature[34,56], confirming that the cDICE approach to prepare GUVs

does not affect their mechanical properties. Additionally, from vesicles in the tension-dominated regime (selected by their radius R_0, which tunes the crossover mode $\bar{\sigma}$) and, hence, showing a clearer ~q^{-1} low-q decay, we also extract a passive membrane tension of $\sigma \approx 10^{-7}$ N m^{-1}, to be considered as an estimate because tension will be different for each GUV and depend on their reduced volume. The spectra of passive vesicles encapsulating MT networks in the absence of ATP, or in the absence of motors and crosslinkers, resemble those observed for bare vesicles (Supplementary Fig. 2b).

By contrast, actively deforming GUVs exhibit fluctuations that are roughly one order of magnitude above the passive reference (Fig. 2f, red) at all mode numbers. From now on, all the spectra refer to the same vesicle with $c_{MT} = 0.8$ mg ml^{-1} MTs, $c_A = 1.5$ μM and $c_K = 120$ nM (further examples showing the effect of parameters variation are shown in Supplementary Fig. 2c and the reproducibility details are given in the Methods). The fluctuation spectra of the active GUVs decay over q similar to the observed passive bending-dominated case: $\langle |u_q|^2 \rangle \approx q^{-3}$. The increase in magnitude indicates that in the presence of activity, thermal excitation of the bending modes of the vesicle is negligible compared with the deformations driven by active forces[28,29,57]. The increase at a high mode number is in part due to the formation of transient tethers, which, however, are rare with respect to the overall smoother deformation.

We then turn to the temporal behaviour of deformations. The time correlation function $\langle u_q(\tau) u_q^*(0) \rangle$ of a purely passive GUV is expected to decay as an exponential[17] with a decay time τ_q, which, in turn, scales exactly like the spatial spectrum, as $\tau_q \approx (q^3 + \bar{\sigma} q)^{-1}$ (Fig. 2g). For active GUVs, however, we observe a $\tau_q \approx 1/q$ scaling at low modes, which does not match the scaling of spatial fluctuations. This indicates that the activity strongly affects the timescales of membrane fluctuations and, thus, defies the relationship between fluctuations and response expected at equilibrium, imposing the same scaling between spatial fluctuations and their temporal decay. Indeed, using previously established methods[58,59], we confirm that membrane fluctuations break detailed balance. Briefly, using the amplitude of Fourier modes as a proxy for the microscopic configuration of GUVs, we find the presence of net probability fluxes Ω in the transitions between different modes, which would be expected to vanish at equilibrium due to the detailed balance. Intriguingly, a statistically significant net flux is only present between some couples of modes, indicating that the active force couples preferentially with deformations of specific wavelengths (Fig. 2h and Supplementary Fig. 4). This confirms that the membrane is out of equilibrium and that its temporal dynamics can be informative about the microscopic details of activity-induced deformations.

MTs set the correlation time of membrane fluctuations

Since the membrane fluctuations are induced by the contained minimal cytoskeleton, we then focus on the properties of MTs inside the GUV, taking advantage of our ability to image them at the same time as the membrane.

With the bundle length (~100 μm) comparable with the GUV diameter (~50 μm), the active network affects the membrane fluctuations, whereas, in turn, the MT organization is altered by the confinement of the membrane. This membrane–cytoskeleton interaction leads to a complex, three-dimensional organization of the bundles (Fig. 3a and Supplementary Video 4). To better show their organization, we tracked bundles using the filament-tracking software SOAX[60] and show that indeed different from previous systems encapsulating active MTs[37], bundles are neither confined on the surface nor do they cover it completely (Fig. 3b).

We identify two main ways in which MTs can push against the membrane. When they extend and push radially against the membrane, they lead to transient, tube-like protrusions ('poking' behaviour; Fig. 3c (top) and Supplementary Video 5). Such tubes are transient and retract. Instead, when the bundles approach the membrane tangentially, they produce long-wavelength deformations, due to bundles buckling against the membrane ('buckling' behaviour; Fig. 3c (bottom) and Supplementary Video 6). In both cases, membrane deformations are closely correlated with the local activity of the MT network.

On the basis of these observations, we postulate that the temporal correlation of membrane deformations is connected to the dynamics of the MT bundles and under the assumption that the activity of filaments is proportional to their number, irrespective of their orientation, we propose to use the local MT density as a proxy for the force they exert. This assumption might be invalid if the filaments push radially and, hence, more effectively; however, we confirm that buckling is the main deformation mode by showing that the bundle orientation $\hat{n}$, extracted using SOAX, is tangential to the membrane when $r \approx R_0$ (Fig. 3d). From fluorescence videos, we then extract the intensity of MTs $\rho(r, \phi, t)$, where r is the distance from the centre of the GUV. We confirm again that filaments can be found in the GUV volume, but filaments are still more concentrated along the membrane surface due to their extensile behaviour; the radial density of MTs peaks at $r \approx R_0$ (Fig. 3e).

Shape changes in the membrane are, hence, driven by the local organization and activity of the MTs, which directly push against the membrane and deform it. We can capture the relevant dynamics of filaments and their interplay with the membrane by reducing our observable to an angular density of MTs $\rho(\phi, t) := \rho(r \approx R_0, \phi, t)$ computed only in the vicinity of the membrane (Fig. 3f). By directly correlating the membrane deformations with the local MT density, we confirm that filaments are also highly concentrated in places where membrane deformations are larger than average (Fig. 3g–h). We then turn to the dynamics of MTs. By tracking the flow of MTs along the membrane (Supplementary Fig. 8a,b), we observed that clusters of highly concentrated MTs travel along the membrane with a speed of $v \approx 1$ μm s^{-1} (Fig. 4a and Supplementary Videos 7 and 8), transporting with them the membrane deformations they induce (Fig. 4b). This gives rise to transient deformation waves that travel, merge or split (Fig. 4c and Supplementary Video 4), and then switch direction or dissolve after around 10 s. These transient waves are due to the tendency of the MT bundles to extend, thereby deforming the membrane. Collision with the membrane deflects the motion of MTs, thereby turning extensile activity into motion along the membrane. On average, the component of the velocity in the direction tangential to the membrane (v_T) accounts for $v_T/v \approx 80\%$ of the total speed (Supplementary Fig. 8c). It follows that the dynamics of the membrane is due to MTs deforming it due to their extensile-based pushing and then moving along the GUV perimeter due to confinement. Consequently, they transport these deformations along the membrane, as confirmed by the correlation between radial deformations, MT density along the membrane and their tangential speed that propagates the deformations (Fig. 4d(i)–d(iii)).

To quantitatively understand the link between MTs and membrane fluctuations, we used again a Fourier series expansion of the MT density $\rho(\phi, t)$. The method mirrors the spectral analysis of membrane, being now focused on the active MT network pushing on the membrane. Briefly, we computed both density fluctuation spectrum $\langle |\rho_q|^2 \rangle$ and its temporal decay for each mode. The fluctuation spectrum (Fig. 4e, blue) is distinct from that of the membrane. This aligns with what we see for an unconfined MT active gel (Supplementary Fig. 7, grey). This suggests that the angular filament density within GUVs is arranged similar to its distribution in bulk. This specific spatial arrangement of MTs, however, when acting on the membrane—although scaling differently than equatorial fluctuations—does influence them, resulting in the observed q-dependent decay of membrane fluctuations. In particular, conversely, the MT density also exhibits q-dependent decay times τ_q^{MT}, which are consistent in both magnitude and scaling with the decay times observed for membrane fluctuations ($\tau_q^{MT} \approx \tau_q$). This parallelism suggests that the active MT fluid determines the membrane fluctuation timescale (Fig. 4f and Supplementary

https://doi.org/10.1038/s41567-025-02839-3

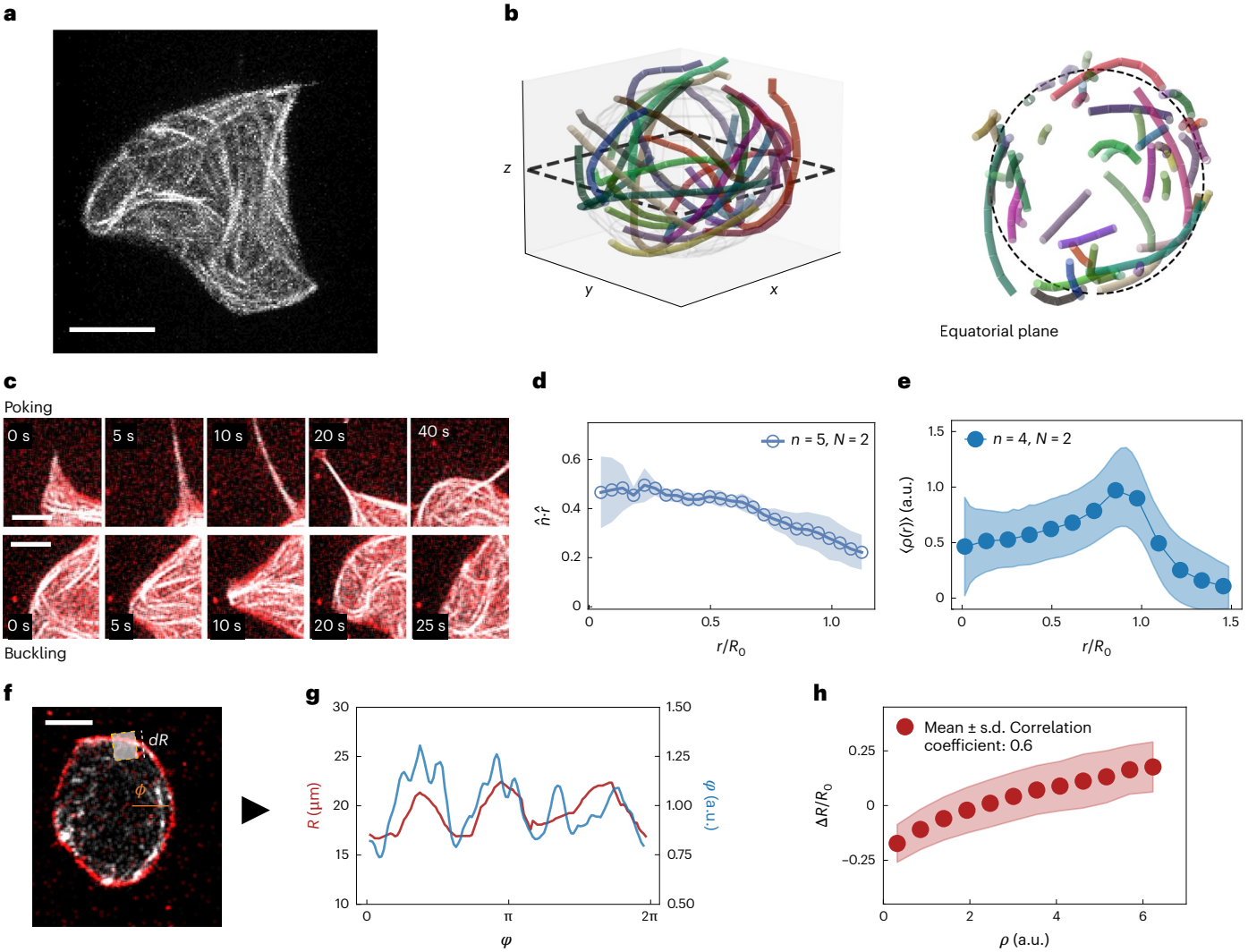

Fig. 3 | MTs act on the membrane to induce shape deformations. a, Confocal projection of the active MT network, showing how its structure is correlated with the GUV shape. Scale bar, 20 μm. Similar results have been obtained for GUVs in similar conditions (Methods). **b**, Tracking of MT bundles inside a GUV using SOAX, from 20 overlaid frames of a confocal recording. The GUV surface is filled with MT bundles (left), but bundles can also be present in unconfined conditions, as shown by a 5-μm-thick slice of the equatorial plane seen from the top (right). Only select bundles are shown, each with a different colour. The dashed line (left) indicates the equatorial plane selected on the right, and the dashed line (right) indicates the average GUV equatorial contour. **c**, Confocal time series, showing how MTs deform the GUV. Bundles can poke the membrane (top), leading to the formation of tubes, or they can (bottom) buckle against the membrane, inducing smoother shape deformations. MTs are marked in white and the membrane, in red. Scale bars, 5 μm. **d**, Close to the surface, MTs are mostly tangential to the membrane, as indicated by the small value of the dot product between the bundle orientation ($\hat{n}$) and radial vector ($\hat{r}$). The shaded area indicates the s.d. between $n = 5$ different GUVs analysed, from $N = 2$ experiments in the same conditions. **e**, Radial intensity profile of the MT density $\rho(r)$, showing accumulation close to the membrane. The dashed line indicates the mean radius of the GUV over time. The shaded area indicates the s.d. between $n = 5$ different GUVs analysed, from $N = 2$ experiments in the same conditions. **f**, MT intensity $\rho(\phi, t)$ is obtained by averaging the MT fluorescence intensity in a box (coloured in yellow) centred at the membrane position $R(\phi, t)$ and with size $dR = 5$ μm (indicated by the white dashed line) to obtain the angular distribution of MTs along the membrane (not to scale in the picture). The angle ϕ is computed using the orange line as a reference ($\phi = 0$). Scale bar, 20 μm. **g**, Plot of the MT density ρ (blue) and the local deformation ΔR (red) along the membrane, showing correlations between the two. A higher density leads to a higher deformation. **h**, Scatter plot of the correlation between the density and deformations along the whole trajectory of a GUV. Deformations are normalized by the mean radius R_0 of the GUV. We find a Pearson correlation coefficient of 0.6, computed using Python's numpy.corrcoef function. The shaded area indicates the s.d. between $n = 5$ different GUVs analysed, from $N = 2$ experiments in the same conditions.

Figs. 5 and 6). This elucidates the observed separation between the membrane's spatial and temporal correlations, the latter being now solely set by the active MT network.

Moreover, again examining a similar MT system in bulk under identical conditions, we found a similar scaling of the correlation times but with faster decay times (around ten times shorter than inside GUVs). This indicates that the confinement induced by the GUV slows down the system dynamics (Fig. 4f, grey). Hence, soft confinement, although not modifying its angular distribution, extends the MT density's correlation timescale. We attribute this effect to the membrane acting as a barrier, which redirects any radial flow of the network tangentially, thereby prolonging its temporal persistence.

Theoretical coarse-grained model recapitulates the observed dynamics

To better understand the behaviour of the temporal and spatial fluctuations of active GUVs, we resort to the numerical simulations of a simplified model that nevertheless captures all the key characteristics

https://doi.org/10.1038/s41567-025-02839-3

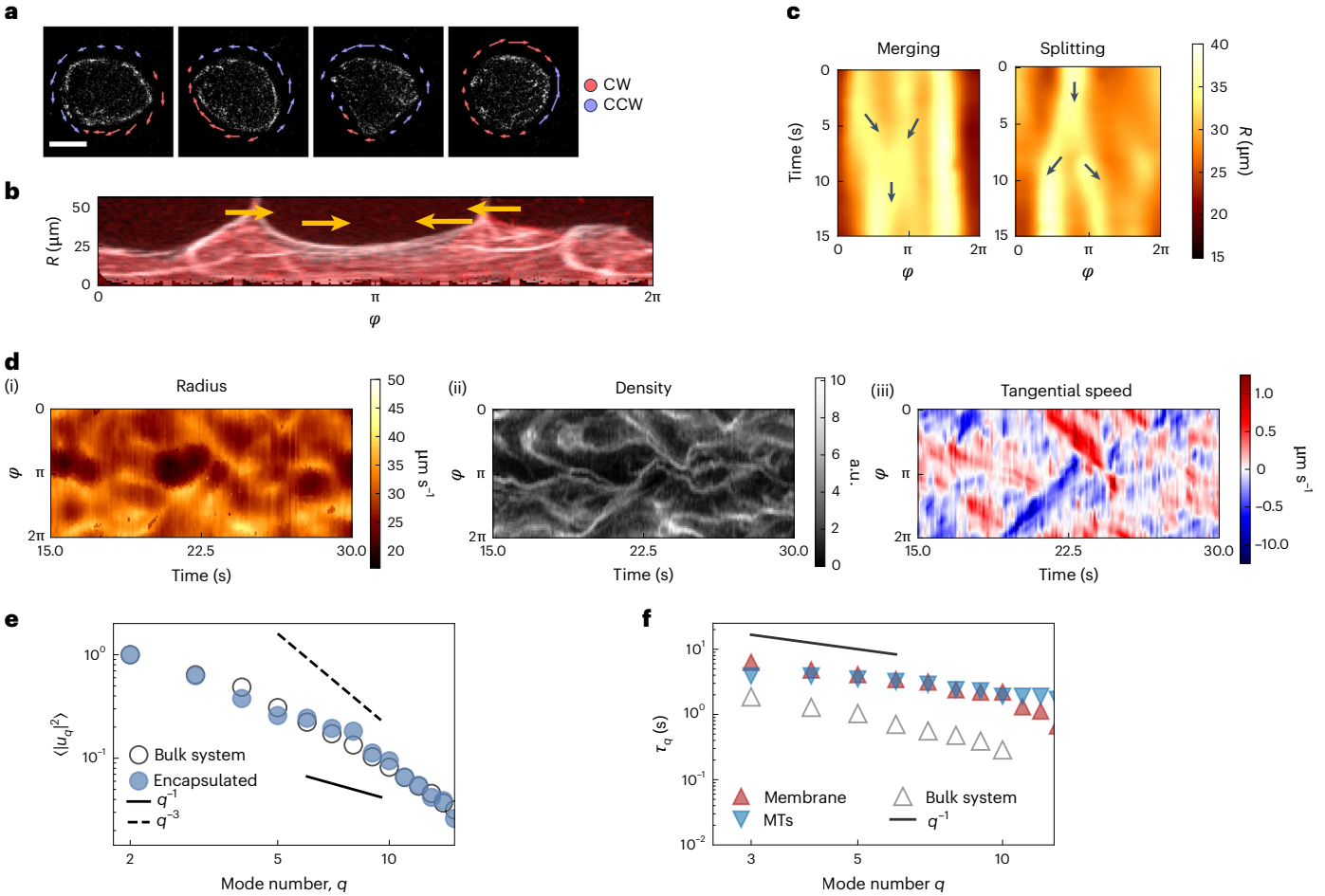

Fig. 4 | Dynamics of MTs sets the dynamics of membrane deformations. **a**, Arrows indicate the tangential component of the speed of MTs in the vicinity of the membrane at four different snapshots of a 6-min recording. The flow goes both clockwise (CW; red) and counterclockwise (CCW; blue), and is organized in domains of similar flow (transient waves) that move, collide and rearrange over time. The arrow colour only indicates the CW/CCW direction. Scale bar, 20 μm. **b**, By visualizing the vesicle using confocal images projected in the (r, ϕ) plane, where r is the distance from the GUV centre, one can see MT-driven membrane deformations that travel along the membrane, transported by the active flow (indicated by arrows). **c**, Kymographs of the membrane deformations $R(\phi, t)$ showing areas of high deformations propagating in time and merging (left) or splitting (right). The arrows indicate the direction of motion. **d**, Kymograph of membrane deformations (i), MT density (ii) and tangential flow along the membrane (iii), showing high correlation and indicating how flow transports the MT density, which, in turn, induces the membrane deformations. **e**, Spatial fluctuation spectrum for the MT density $\rho(\phi)$ both under GUV confinement but close to the membrane (full blue circles) and in unconfined conditions (open grey circles). Both spectra are normalized so that they have a value of 1 at $q = 2$. The two quantities show a similar decay. As shown in Fig. 2g, the dashed line indicates a q^{-3} scaling and the solid black line, a q^{-1} scaling. **f**, Correlation times τ_q of deformations at each mode q for the membrane (red) compared with those extracted from the spectral description of the MT density $\rho(\phi, t)$ (blue). The two curves are comparable with each other and display the same scaling. The same spectral analysis, performed on the unconfined system, shows a similar scaling but faster decorrelation. The solid black line shows a q^{-1} scaling.

of the experimental system. We implement a fluid membrane model based on dynamically triangulated surfaces[61,62], consisting of a mesh of membrane points connected by bonds. The vesicle membrane has a diameter $D = 40$ μm, area and volume conservation are enforced (Supplementary Section 3), and we set the membrane bending rigidity and tension to $\kappa = 20 k_B T$ and $\sigma = 10^{-8}$ N m^{-1}, respectively. Membrane hydrodynamics is ignored for simplicity, but this does not significantly affect the results (Supplementary Fig. 10e). The active cytoskeleton is implemented by a set of $N_{fil} = 20$ filaments placed inside the vesicle. Filaments have a relaxed length $L = D/2$ and can grow and extend for a typical time T_{str} to reach a maximum length $L_{max} = 2D$, before shrinking back. This growth dynamics simulates the extensile behaviour of MT bundles and their ability to buckle, whereas the shrinking simulates bundles breaking and/or leaving the membrane. Bundle activity leads to membrane deformations analogous to the experimentally observed ones (Supplementary Video 9 and Fig. 5a,b). Kymographs of the membrane deformations for different values of T_{str} show the 'wave-like' behaviour observed in experiments if T_{str} is high enough, indicating that filaments transport deformations in space by extending along the membrane. Conversely, for low T_{str}, membrane deformations are only local and, as the filaments shrink, quickly relax with their passive decay time (Fig. 5b). We find good agreement between the simulated vesicles and the experimental measurements, both for passive and active GUVs and in both spatial and temporal decays of fluctuations (Fig. 5c). The simulated fluctuation spectrum is indeed roughly one order of magnitude higher than the passive reference and scales indicatively as $\sim q^{-3}$ (Fig. 5c, top), whereas the relaxation time of the membrane deviates from the equilibrium behaviour and shows a q^{-1} decay (Fig. 5c, bottom), in accordance with the experimental findings. We postulated that this behaviour of active vesicles arises whenever activity dominates the membrane dynamics, that is, if $T_{str} > \tau_q^P$, where τ_q^P is the passive relaxation time of the membrane. Indeed, if $T_{str} \ll \tau_q^P$, the temporal relaxation is marginally affected, whereas for $T_{str} \gg \tau_q^P$, the membrane relaxation is fully driven by activity, exhibiting the peculiar q^{-1} scaling and overall increasing

https://doi.org/10.1038/s41567-025-02839-3

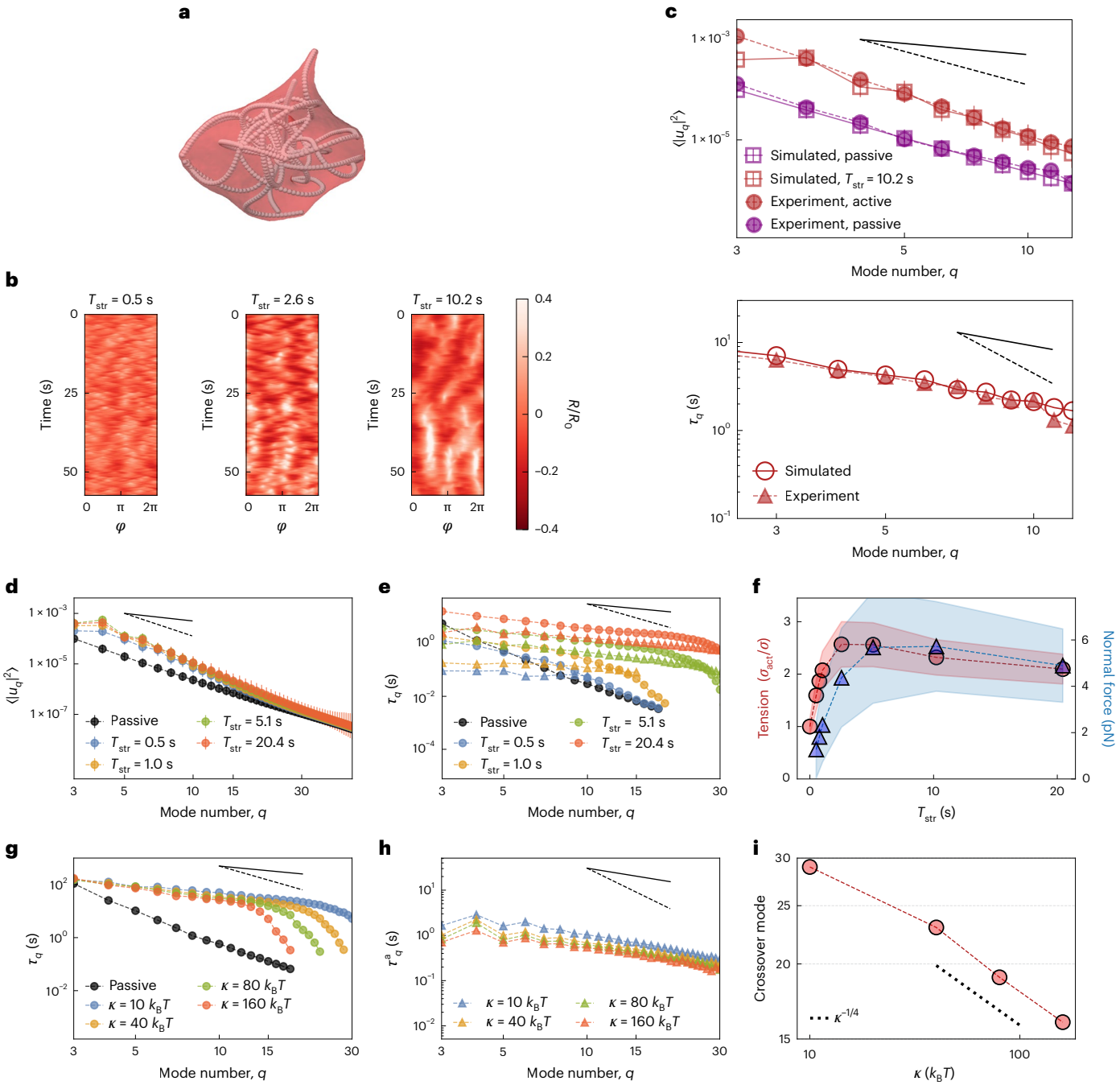

Fig. 5 | Simulations recover and extend the experimental results. a, Snapshot of numerical simulations, carried out for $T_{str} = 10.2$ s. Extensile filaments (white) are shown inside a simulated membrane (red) and deform it. **b**, Kymographs of equatorial membrane deformations (R is the distance from the GUV centre at a given angle ϕ) at different values of extension time T_{str}, normalized by the mean radius R_0. **c**, Top: spatial fluctuation spectrum of passive (purple) and active (red) membranes, from experiments (full circles) and simulations (empty squares; extension time, $T_{str} = 10.2$ s for the active case) showing similar scaling and magnitude. **c**, Bottom: simulated (empty circles) and experimental (full triangles) correlation times τ_q for each mode q for the active case, in the same conditions. In this and the subsequent plots, a dashed black line indicates an $\sim q^{-3}$ scaling and a solid black line, an $\sim q^{-1}$ one. The error estimate (mean ± s.d.) for simulations is explained in the Methods. **d**, Simulated spatial fluctuations at different values of T_{str}, with passive reference in black, showing that the temporal dynamics of the force does not significantly affect the active spectrum. Error estimate (mean ± s.d.) for simulations is explained in the Methods. In **c** and **d**, the experimental and simulation errors are computed as explained in the Methods. **e**, Simulated temporal fluctuations of the membrane (τ_q; circles) and of the active force (τ_q^a; triangles) at different values of T_{str}, with the passive reference (τ_q^p) shown in black. Both force and membrane show the observed q^{-1} decay. **f**, Simulated tension σ_{act} and mean force acting on the membrane at different values of T_{str}, showing a limited increase in both quantities. Mean ± s.d. are shown. **g**, Temporal fluctuations of the membrane at different values of κ with the passive reference, showing how rigidity affects only the low-q modes **h**, Simulated temporal fluctuations of the force (τ_q^a) at different values of κ, with the passive reference shown in black. The bending rigidity κ does not significantly alter the temporal properties of the active force. **i**, Crossover mode at which the active temporal fluctuations stop scaling as q^{-1} as a function of κ. The dotted line indicates the scaling with the bending rigidity as $\kappa^{-1/4}$, compatible with the energy cost of bending a membrane.

correlation time as T_{str} grows (Fig. 5e, circles). By measuring the correlation time at each mode of the active force τ_q^a (Supplementary Section 2), we again show that the $\sim q^{-1}$ decay of the membrane correlation times is imposed by the temporal activity of the force (Fig. 5e, triangles). Interestingly, we observe this temporal scaling for different values of N_{fil}, L_{max}/D and the vesicle's reduced volume (Supplementary Fig. 10). By contrast, the behaviour of the fluctuation spectrum is only mildly affected by all of the above parameters, indicating that the temporal behaviour of the membrane fluctuations, rather than its spatial counterpart, might be a better readout of the effect of activity. We then looked at a possible explanation for this behaviour. As $\sim q^{-1}$ decays are commonly associated with tension, we wondered whether the observed scaling could be explained in terms of an effective active tension σ_{act} by pushing forces[14,22]. We found that as T_{str} increases, the total tension indeed rises. At the same time, the mean active force acting on the membrane also increases (Fig. 5f). However, the effect is small, with only a moderate increase in tension due to the active force. We then tested the effect of membrane rigidity κ. As κ increases from $10k_BT$ to $160k_BT$ at fixed $T_{str} = 10.2$ s, the same $\sim q^{-1}$ scaling is observed, but only at lower modes, indicating an interplay between membrane mechanical properties and the active force (Fig. 5g). This effect, in which the membrane and the active force synchronize only at low modes, is not dependent on a change in the temporal correlation of the force, which is not modified by the bending rigidity (Fig. 5h) but depends only on the mechanical properties of the membrane. Indeed, the crossover mode at which the $\sim q^{-1}$ behaviour stops scales as $\sim \kappa^{-1/4}$, that is, the highest excitable mode is the one at which the force becomes comparable with the cost of bending deformations $\sim \kappa q^4$ (Fig. 5i). Hence, an additional condition for the synchronization to happen is that the force is stronger than the membrane's deformation cost. We conclude that this behaviour is universal, as we consistently observed an $\sim q^{-1}$ scaling in the membrane's temporal relaxation as soon as activity dominates. The tight correlation between membrane deformation and force is confirmed in simulations, indicating that the behaviour of the membrane follows the behaviour of the filaments in the temporal domain. The observed fluctuations in the membrane and MT dynamics, hence, reflect a feedback in which soft confinement modifies the temporal MT organization, which, in turn, dictates large membrane fluctuations around the equilibrium spherical shape. The resulting activity of the MT network acting on the membrane is correlated in time and drives the dynamics of membrane fluctuations accordingly, as can be rationalized by the fact that the correlation function of a membrane under the effect of active correlated noise tends to synchronize with the slower timescale[13,14,24], which is the active one here. Measuring both quantities directly allows to clearly prove it.

In summary, deformation dynamics are regulated by active forces, with temporal fluctuations better capturing out-of-equilibrium signatures than spatial ones[13,14,24,26,27] and, hence, being a more direct observable of activity in living systems. Membrane deformations also allow to extract the typical time and force of the active system. Our system relies on a simplified cell and cytoskeleton model, whereas in cells, membrane deformations are rather a consequence of actin turnover dynamics. However, experiments recover typical timescales and mechanical properties of living cells. Additionally, GUVs also represent a model for protocells; hence, similar active fluctuations might shed light on early organizations of biomembranes. Although extreme, the deformations we observe do not lead to any transition from a spherical topology, which would be possible by including area growth, bringing it closer to origin-of-life conditions reported elsewhere[10]. Overall, understanding this dynamics is, therefore, a fundamental step in the programs of understanding biomembrane deformations and of reconstituting a realistic synthetic cell.

Online content

Any methods, additional references, Nature Portfolio reporting summaries, source data, extended data, supplementary information, acknowledgements, peer review information; details of author contributions and competing interests; and statements of data and code availability are available at https://doi.org/10.1038/s41567-025-02839-3.

References

1. Ofer, N., Mogilner, A. & Keren, K. Actin disassembly clock determines shape and speed of lamellipodial fragments. *Proc. Natl Acad. Sci. USA* **108**, 20394–20399 (2011).
2. Pollard, T. D. & Cooper, J. A. Actin, a central player in cell shape and movement. *Science* **326**, 1208–1212 (2009).
3. Needleman, D. & Dogic, Z. Active matter at the interface between materials science and cell biology. *Nat. Rev. Mater.* **2**, 17048 (2017).
4. Steinkühler, J. et al. Controlled division of cell-sized vesicles by low densities of membrane-bound proteins. *Nat. Commun.* **11**, 905 (2020).
5. Szostak, J. W., Bartel, D. P. & Luisi, P. L. Synthesizing life. *Nature* **409**, 387–390 (2001).
6. Goldstein, R. E. & van de Meent, J.-W. A physical perspective on cytoplasmic streaming. *Interface Focus* **5**, 20150030 (2015).
7. Liu, A. P. et al. Membrane-induced bundling of actin filaments. *Nat. Phys.* **4**, 789–793 (2008).
8. Blanchoin, L., Boujemaa-Paterski, R., Sykes, C. & Plastino, J. Actin dynamics, architecture, and mechanics in cell motility. *Physiol. Rev.* **94**, 235–263 (2014).
9. Almonacid, M. et al. Active fluctuations of the nuclear envelope shape the transcriptional dynamics in oocytes. *Dev. Cell* **51**, 145–157 (2019).
10. Ruiz-Herrero, T., Fai, T. G. & Mahadevan, L. Dynamics of growth and form in prebiotic vesicles. *Phys. Rev. Lett.* **123**, 038102 (2019).
11. Brochard, F., Lennon, J. F. & Erythrocytes, I. N. Frequency spectrum of the flicker phenomenon in erythrocytes. *J. Phys.* **36**, 1035–1047 (1975).
12. Strey, H., Peterson, M. & Sackmann, E. Measurement of erythrocyte membrane elasticity by flicker eigenmode decomposition. *Biophys. J.* **69**, 478–488 (1995).
13. Monzel, C. et al. Measuring fast stochastic displacements of bio-membranes with dynamic optical displacement spectroscopy. *Nat. Commun.* **6**, 8162 (2015).
14. Turlier, H. & Betz, T. Unveiling the active nature of living-membrane fluctuations and mechanics. *Annu. Rev. Condens. Matter Phys.* **10**, 213–232 (2019).
15. Zidovska, A. & Sackmann, E. Brownian motion of nucleated cell envelopes impedes adhesion. *Phys. Rev. Lett.* **96**, 048103 (2006).
16. Monzel, C. & Sengupta, K. Measuring shape fluctuations in biological membranes. *J. Phys. D: Appl. Phys.* **49**, 243002 (2016).
17. Faizi, H. A., Reeves, C. J., Georgiev, V. N., Vlahovska, P. M. & Dimova, R. Fluctuation spectroscopy of giant unilamellar vesicles using confocal and phase contrast microscopy. *Soft Matter* **16**, 8996–9001 (2020).
18. Dimova, R. & Marques, C. (eds) *The Giant Vesicle Book* 1st edn (CRC Press, 2019).
19. Gracià, R. S., Bezlyepkina, N., Knorr, R. L., Lipowsky, R. & Dimova, R. Effect of cholesterol on the rigidity of saturated and unsaturated membranes: fluctuation and electrodeformation analysis of giant vesicles. *Soft Matter* **6**, 1472–1482 (2010).
20. Helfrich, W. Elastic properties of lipid bilayers: theory and possible experiments. *Z. Naturforsch. C* **28**, 693–703 (1973).
21. Canham, P. B. The minimum energy of bending as a possible explanation of the biconcave shape of the human red blood cell. *J. Theor. Biol.* **26**, 61–81 (1970).
22. Loubet, B., Seifert, U. & Lomholt, M. A. Effective tension and fluctuations in active membranes. *Phys. Rev. E* **85**, 031913 (2012).
23. Gov, N., Zilman, A. G. & Safran, S. Cytoskeleton confinement and tension of red blood cell membranes. *Phys. Rev. Lett.* **90**, 228101 (2003).

24. Bouvrais, H., Cornelius, F., Ipsen, J. H. & Mouritsen, O. G. Intrinsic reaction-cycle time scale of Na+,K+-ATPase manifests itself in the lipid-protein interactions of nonequilibrium membranes. *Proc. Natl Acad. Sci. USA* **109**, 18442–18446 (2012).
25. Almendro-Vedia, V. G. et al. Nonequilibrium fluctuations of lipid membranes by the rotating motor protein F_1F_0-ATP synthase. *Proc. Natl Acad. Sci. USA* **114**, 11291–11296 (2017).
26. Rodríguez-García, R. et al. Direct cytoskeleton forces cause membrane softening in red blood cells. *Biophys. J.* **108**, 2794–2806 (2015).
27. Betz, T., Lenz, M., Joanny, J.-F. J. F. & Sykes, C. ATP-dependent mechanics of red blood cells. *Proc. Natl Acad. Sci. USA* **106**, 15320–15325 (2009).
28. Vutukuri, H. R. et al. Active particles induce large shape deformations in giant lipid vesicles. *Nature* **586**, 52–56 (2020).
29. Takatori, S. C. & Sahu, A. Active contact forces drive nonequilibrium fluctuations in membrane vesicles. *Phys. Rev. Lett.* **124**, 158102 (2020).
30. Peterson, M. S. E., Baskaran, A. & Hagan, M. F. Vesicle shape transformations driven by confined active filaments. *Nat. Commun.* **12**, 7247 (2021).
31. Park, M., Lee, K. & Granick, S. Response of vesicle shapes to dense inner active matter. *Soft Matter* **18**, 6419–6425 (2022).
32. Iyer, P., Gompper, G. & Fedosov, D. A. Non-equilibrium shapes and dynamics of active vesicles. *Soft Matter* **18**, 6868–6881 (2022).
33. Prost, J. & Bruinsma, R. Shape fluctuations of active membranes. *Europhys. Lett.* **33**, 321–326 (1996).
34. Pécréaux, J., Döbereiner, H.-G., Prost, J., Joanny, J.-F. J.-F. & Bassereau, P. Refined contour analysis of giant unilamellar vesicles. *Eur. Phys. J. E* **13**, 277–290 (2004).
35. Pécréaux, J., Döbereiner, H.-G., Prost, J., Joanny, J.-F. & Bassereau, P. Refined contour analysis of giant unilamellar vesicles. *Eur. Phys. J. E* **13**, 277–290 (2004).
36. Loiseau, E. et al. Shape remodeling and blebbing of active cytoskeletal vesicles. *Sci. Adv.* **2**, e1500465 (2016).
37. Keber, F. C. et al. Topology and dynamics of active nematic vesicles. *Science* **345**, 1135–1139 (2014).
38. Hsu, C.-P., Sciortino, A., de la Trobe, Y. A. & Bausch, A. R. Activity-induced polar patterns of filaments gliding on a sphere. *Nat. Commun.* **13**, 2579 (2022).
39. Tsai, F.-C., Stuhrmann, B. & Koenderink, G. H. Encapsulation of active cytoskeletal protein networks in cell-sized liposomes. *Langmuir* **27**, 10061–10071 (2011).
40. Mulla, Y., Aufderhorst-Roberts, A. & Koenderink, G. H. Shaping up synthetic cells. *Phys. Biol.* **15**, 041001 (2018).
41. Baldauf, L., Van Buren, L., Fanalista, F. & Koenderink, G. H. Actomyosin-driven division of a synthetic cell. *ACS Synth. Biol.* **11**, 3120–3133 (2022).
42. Baldauf, L., Frey, F., Perez, M. A., Idema, T. & Koenderink, G. H. Branched actin cortices reconstituted in vesicles sense membrane curvature. *Biophys. J.* **122**, 2311–2324 (2023).
43. Tsai, F.-C., Roth, S., Dogterom, M. & Koenderink, G. H. Biomimetic liposome model systems to study cell shape control by the cytoskeleton. *Adv. Planar Lipid Bilayers Liposomes* **19**, 139–173 (2014).
44. Chen, S., Sun, Z. G. & Murrell, M. P. In vitro reconstitution of the actin cytoskeleton inside giant unilamellar vesicles. *J. Vis. Exp.* **186**, e64026 (2022).
45. Tsai, F.-C. et al. Activated I-BAR IRSp53 clustering controls the formation of VASP-actin-based membrane protrusions. *Sci. Adv.* **8**, eabp8677 (2022).
46. Beber, A. et al. Membrane reshaping by micrometric curvature sensitive septin filaments. *Nat. Commun.* **10**, 420 (2019).
47. Sakamoto, R., Izri, Z., Shimamoto, Y., Miyazaki, M. & Maeda, Y. T. Geometric trade-off between contractile force and viscous drag determines the actomyosin-based motility of a cell-sized droplet. *Proc. Natl Acad. Sci. USA* **119**, e2121147119 (2022).
48. Henkin, G., DeCamp, S. J., Chen, D. T. N., Sanchez, T. & Dogic, Z. Tunable dynamics of microtubule-based active isotropic gels. *Phil. Trans. R. Soc. A* **372**, 20140142 (2014).
49. Sanchez, T., Chen, D. T., Decamp, S. J., Heymann, M. & Dogic, Z. Spontaneous motion in hierarchically assembled active matter. *Nature* **491**, 431–434 (2012).
50. Adkins, R. et al. Dynamics of active liquid interfaces. *Science* **377**, 768–772 (2022).
51. Chandrakar, P. et al. Engineering stability, longevity, and miscibility of microtubule-based active fluids. *Soft Matter* **18**, 1825–1835 (2022).
52. Berezney, J., Goode, B. L., Fraden, S. & Dogic, Z. Extensile to contractile transition in active microtubule-actin composites generates layered asters with programmable lifetimes. *Proc. Natl Acad. Sci. USA* **119**, e2115895119 (2022).
53. Abkarian, M., Loiseau, E. & Massiera, G. Continuous droplet interface crossing encapsulation (cDICE) for high throughput monodisperse vesicle design. *Soft Matter* **7**, 4610–4614 (2011).
54. Van de Cauter, L. et al. Optimized cDICE for efficient reconstitution of biological systems in giant unilamellar vesicles. *ACS Synth. Biol.* **10**, 1690–1702 (2021).
55. Duclos, G. et al. Topological structure and dynamics of three-dimensional active nematics. *Science* **367**, 1120–1124 (2020).
56. Roux, A. et al. Membrane curvature controls dynamin polymerization. *Proc. Natl Acad. Sci. USA* **107**, 4141–4146 (2010).
57. Manneville, J.-B., Bassereau, P., Ramaswamy, S. & Prost, J. Active membrane fluctuations studied by micropipet aspiration. *Phys. Rev. E* **64**, 021908 (2001).
58. Battle, C. et al. Broken detailed balance at mesoscopic scales in active biological systems. *Science* **352**, 604–607 (2016).
59. Kokot, G., Faizi, H. A., Pradillo, G. E., Snezhko, A. & Vlahovska, P. M. Spontaneous self-propulsion and nonequilibrium shape fluctuations of a droplet enclosing active particles. *Commun. Phys.* **5**, 91 (2022).
60. Xu, T. et al. SOAX: a software for quantification of 3D biopolymer networks. *Sci. Rep.* **5**, 9081 (2015).
61. Kroll, D. M. & Gompper, G. The conformation of fluid membranes: Monte Carlo simulations. *Science* **255**, 968–971 (1992).
62. Gompper, G. & Kroll, D. M. in *Statistical Mechanics of Membranes and Surfaces* 2nd edn (eds Nelson, D. R., Piran, T. & Weinberg, S.) 359–426 (World Scientific, 2004).

Methods

Buffers and proteins

M2B is 80 mM PIPES (pH 6.8), 2 mM $MgCl_2$ and 1 mM EGTA. 3.2 mM $MgCl_2$ is added at the end from a 67 stock already diluted in M2B.

Lipids (Texas Red DHPE and DOPC, Avanti Polar Lipids) are bought from Thermo Fisher. Anillin is purified in the laboratory from its sequence (Supplementary Section 1). Silicon and mineral oil are purchased from Sigma.

Encapsulation using cDICE

Vesicles are produced using the cDICE method[38,53,54] consisting briefly of letting droplets of the active mixture cross a layer of oil (silicon and mineral oil; Sigma) containing lipids, to coat them with a membrane. The droplets are produced by inserting a capillary in a three-dimensionally printed rotating chamber[38]. Finally, the vesicles accumulate in a buffered aqueous solution, whose osmolarity is matched to 20 mOsm kg^{-1} higher than the active mix using glucose. The mixture is prepared as follows: the desired concentration of stabilized MTs is mixed in M2B together with the desired concentration of kinesins, anillin and 2 mM ATP. The mixture also contains a scavenging system (10 U ml^{-1} glucose oxidase and 1 kU ml^{-1} catalase; Sigma), glucose (3 mg ml^{-1}), an ATP regeneration system (18.2 U ml^{-1} of creatine phosphokinase and 9 mM of creatine phosphate; Sigma) and 5 mM dithiothreitol. It is ensured that the final concentration of salts is exactly the one expected for M2B by correcting using a 10× M2B preparation. The stock of MTs and the mixture are kept at room temperature to avoid depolymerization. After mixing, we wait for 5 min for the active fluid to assemble. Its osmotic pressure is measured using a Gondotec osmometer, and a buffered solution, containing glucose, with comparable osmotic pressure is also prepared. Finally, the cDICE encapsulation is carried out at room temperature. We use a capillary with a diameter of 40 µm to allow for big vesicles and fast encapsulation (5 min). The vesicles are then harvested, transferred to a glass coverslip coated with 1 mg ml^{-1} bovine serum albumin (Sigma) and observed under a microscope.

Imaging

Vesicles are acquired using a confocal microscope (Leica DMi5, ×63 objective, 1.4 numerical aperture; LAS X, acquisition software) equipped with a resonant scanner. Long time series of the equatorial plane are acquired using a 256 × 256 image size with a time interval of 35–250 ms (around 4,000 frames, for a total recording time of 5–10 min per GUV). The pinhole was set to 1 Airy unit. Both membrane and MT channel are acquired at the same time. Three-dimensional stacks are also acquired at different resolutions and time intervals.

Extraction of GUV contour and MT density

The images of the membrane channel are thresholded and the GUV contour is obtained using custom-written Python 3, MATLAB (version R2024) and Mathematica codes. Briefly, using the centre of the GUV as a reference, the space is divided in overlapping angular segments of amplitude $da = 0.25$ rad and separated by $d\phi = 0.15$, inside which the radial position of the point with the maximum intensity of the membrane is found, thereby obtaining a discretization of $R(\phi)$. The same logic is applied to the MT intensity to obtain $\rho(\phi, r)$, which can then be averaged inside a box of width da and contained between $R(\phi)$ and $R(\phi) - dR$ with $dR = 5$ µm to obtain $\rho(\phi)$ in proximity of the membrane.

Kurtosis analysis

The extracted contours are split in a series of lengths τ_{avg}; from each series, the histogram of the deformations $(R - R_0)/R_0$ (where R_0 is the mean radius of the GUV over time) is extracted. The kurtosis for each resulting distribution is then computed and normalized so that the expected value for a Gaussian is 0 (excess kurtosis). For each value of τ_{avg}, we then obtain a list of kurtosis collected and from which their average, standard deviation (s.d.), and minimum and maximum values are computed.

Fluctuation spectra and decay times

The discretized version of $R(\phi)$ and $\rho(\phi)$ are, at each time point, expanded in a Fourier series to obtain the complex coefficients $u_q(t)$. For this, we compute the integrals $a_q(t) = (1/\pi)\int R(\phi, t)\sin(q\phi)\mathrm{d}\phi$ and $b_q(t) = (1/\pi)\int R(\phi, t)\cos(q\phi)\mathrm{d}\phi$, using the trapezoidal rule. From this, we obtain $u_q(t) = (-a_q(t), b_q(t))$. Alternatively, $R(\phi, t)$ is Fourier transformed with a fast Fourier transform to obtain the complex coefficients $u_q(t)$, appropriately scaled to match the mode number q. The variance of $u_q(t)$ yields the spatial spectrum, whereas its correlation function is used to extract the decay times. The decay time is defined as the time at which the correlation decreases below $1/e$ of the initial value to compare decays that are not strictly speaking exponentials.

Statistics and reproducibility

Given the complexity and the large variation between vesicles, data are not pooled together, and only one GUV is shown in the text. The error bars on the individual spectra are obtained using the standard error of the mean from contour detection, based on the optical resolution of the camera. Other GUVs in the same conditions shown in the main text are discussed in Supplementary Figs. 2 and 3, including data on the GUV-to-GUV and day-to-day reproducibility of the experiment. Vesicles in different conditions are shown in Supplementary Fig. 1. Qualitatively, all the observed GUVs show the same trends, that is, an enhanced fluctuation spectrum and a synchronization between membrane and MT density in time. GUVs containing the active fluid but not showing active behaviour were excluded from the analysis and attributed to a faulty encapsulation process. No randomization or blinding was used. Errors in the simulation are computed as the mean ± s.d. of the quantities over 16,500 snapshots.

Broken detailed balance

We extract the microscopic configurations of GUVs by decomposing their contours into different Fourier modes. The resulting (discretized) Fourier coefficients act as a proxy for a given configuration, and the probability of a given configuration is defined as the ratio of the time spent with a given set of Fourier coefficients over the toal time of the acquisition. The currents across the box boundaries determined by counting statistics, that is, the transitions between boxes yields the the probability current $\mathbf{j}$. A non-zero value of its contour integral $\Omega = \frac{\oint_C \mathbf{j}\cdot\mathrm{d}\mathbf{l}}{\oint_C |\mathbf{j}|\,\mathrm{d}l}$ indicates a system out of equilibrium, where C is a cycle. The flux is normalized and, hence, dimensionless. More details about this method are provided elsewhere[58,59]. The z score of each flux is obtained by collecting all the values of Ω across different cycles, taking their average and checking how many s.d. values away from $\Omega = 0$ it is.

Bundle tracking

Bundles are tracked using SOAX[60] based on active contours. Confocal stacks of active GUVs are analysed, and the bundle contour segmented in positions $\mathbf{r}_i$ is extracted and plotted in three dimensions. Their local orientation is given by $\mathbf{n}_i = \mathbf{r}(i+1) - \mathbf{r}_i$, enabling to find their alignment with respect to the radial direction. As $\mathbf{n}_i$ and $-\mathbf{n}_i$ are equivalent, the alignment is chosen to have a positive radial component.

Analysis of MT flow

To extract the flow of MTs inside GUVs, the videos of the MT channel at the equatorial plane are analysed using an optical flow algorithm using a custom Python 3 script. Roughly, the intensity is followed over time extracting its flow, and then, the flow close to the membrane (using the procedure detailed above for the MT density) is averaged over 1 s and decomposed into tangential and radial components by a scalar product with a unit vector starting from the centre of the GUV and extending radially and its normal counterpart (tangential).

Bulk experiments

To perform bulk (unconfined) experiments, the same mixture is injected inside a 10-µl microscopy chamber composed of a glass slide

and a coverslip separated by a layer of parafilm. The slides and coverslips are passivated using polyacrylamide[52]. The Fourier analysis of the unconfined fluid is detailed in Supplementary Section 2.6.

Coarse-grained modelling

In simulations, the membrane is modelled as a two-dimensional dynamically triangulated network, in which bonds between neighbouring vertices can be cut, flipped and reattached to mimic the internal reorganization of a fluid lipid bilayer. The extensile MT bundles are described by linear bead-spring chains with bending rigidity. The extension/retraction is described by a linear temporal growth of the bond lengths. The interaction of the filaments with the membrane is taken to be purely repulsive. Details and parameters are given in Supplementary Section 3.

Reporting summary

Further information on research design is available in the Nature Portfolio Reporting Summary linked to this article.

Data availability

All raw data used in the Article are available via Zenodo (https://doi.org/10.5281/zenodo.11351857)[63], which includes source data for the images and plots in the main text.

Code availability

Scripts used for the analysis of the data are available via Zenodo (https://doi.org/10.5281/zenodo.11351857)[63]. The membrane model used for simulating the membrane is available from the corresponding author G.G. upon reasonable request.

References

63. Sciortino, A. et al. Active membrane deformations of a minimal synthetic cell. *Zenodo* https://doi.org/10.5281/zenodo.11351857 (2025).

Acknowledgements

A.S. and A.R.B. acknowledge support from the European Research Council (ERC) under the European Union's Horizon 2020 research and innovation programme (grant agreement no. 810104-PoInt, to A.B.). L.F. acknowledges NSF MRSEC, DMR-2011846. We also acknowledge computational support from NSF XSEDE computing resources allocation TG-MCB090163 (Expanse, Anvil and Bridges-2) and the Brandeis HPCC, which is partially supported by the NSF through DMR-MRSEC 2011846 (to L.F.) and OAC-1920147 (to L.F.). A.S. and A.R.B. acknowledge the Brandeis MRSEC for shipping the MTs and kinesin (grant no. MRSEC-DMR-2011846). We thank P. Bleicher for help with the purification of anillin. D.A.F. and G.G. appreciate the computing time on the supercomputer JURECA at Forschungszentrum Jülich (grant acronym: actsys). P.M.V. and H.A.F. acknowledge financial support from NIH award no. 1R01GM140461. This research was also supported in part by the NSF under grant no. PHY-1748958.

Author contributions

A.S. designed and performed the experiments, analysed the data and wrote the manuscript. H.A.F. designed the research, analysed the data and wrote the manuscript. D.A.F. and G.G. designed the theoretical model, performed the simulations and analysed the results, with the collaboration of L.F. P.M.V. assisted with the analysis of membrane fluctuations. A.R.B. designed the research and wrote the manuscript. All authors revised the manuscript.

Funding

Open access funding provided by Technische Universität München.

Competing interests

The authors declare no competing interests.

Additional information

Supplementary information The online version contains supplementary material available at https://doi.org/10.1038/s41567-025-02839-3.

Correspondence and requests for materials should be addressed to Gerhard Gompper or Andreas R. Bausch.

Peer review information *Nature Physics* thanks Kheya Sengupta and the other, anonymous, reviewer(s) for their contribution to the peer review of this work.

nature portfolio

Corresponding author(s): Andreas Bausch, Gerhald Gompper

Last updated by author(s): Sciortino, Bausch, 12 Jan 2025

Reporting Summary

Nature Portfolio wishes to improve the reproducibility of the work that we publish. This form provides structure for consistency and transparency in reporting. For further information on Nature Portfolio policies, see our Editorial Policies and the Editorial Policy Checklist.

Statistics

For all statistical analyses, confirm that the following items are present in the figure legend, table legend, main text, or Methods section.

n/a	Confirmed
☐	☒ The exact sample size (*n*) for each experimental group/condition, given as a discrete number and unit of measurement
☐	☒ A statement on whether measurements were taken from distinct samples or whether the same sample was measured repeatedly
☐	☒ The statistical test(s) used AND whether they are one- or two-sided *Only common tests should be described solely by name; describe more complex techniques in the Methods section.*
☒	☐ A description of all covariates tested
☒	☐ A description of any assumptions or corrections, such as tests of normality and adjustment for multiple comparisons
☐	☒ A full description of the statistical parameters including central tendency (e.g. means) or other basic estimates (e.g. regression coefficient) AND variation (e.g. standard deviation) or associated estimates of uncertainty (e.g. confidence intervals)
☒	☐ For null hypothesis testing, the test statistic (e.g. *F*, *t*, *r*) with confidence intervals, effect sizes, degrees of freedom and *P* value noted *Give P values as exact values whenever suitable.*
☒	☐ For Bayesian analysis, information on the choice of priors and Markov chain Monte Carlo settings
☒	☐ For hierarchical and complex designs, identification of the appropriate level for tests and full reporting of outcomes
☒	☐ Estimates of effect sizes (e.g. Cohen's *d*, Pearson's *r*), indicating how they were calculated

Our web collection on statistics for biologists contains articles on many of the points above.

Software and code

Policy information about availability of computer code

Data collection	Data has been collected with a Leica confocal and LAS X software.
Data analysis	Data analysis has been carried out with custom scripts in Python3 and Matlab R2024 (custom scripts found at 10.5281/zenodo.1135185). Further analysis has been done with SOAX v3.6.0. All scripts used for the analysis of the data are included in the Zenodo repository (10.5281/zenodo.11351857). The membrane model used for simulating membrane is available upon reasonable request

For manuscripts utilizing custom algorithms or software that are central to the research but not yet described in published literature, software must be made available to editors and reviewers. We strongly encourage code deposition in a community repository (e.g. GitHub). See the Nature Portfolio guidelines for submitting code & software for further information.

Data

Policy information about availability of data

All manuscripts must include a data availability statement. This statement should provide the following information, where applicable:

- Accession codes, unique identifiers, or web links for publicly available datasets
- A description of any restrictions on data availability
- For clinical datasets or third party data, please ensure that the statement adheres to our policy

DATA AVAILABILITY STATEMENT: All raw data used for the manuscript is available in a Zenodo repository (10.5281/zenodo.11351857). This includes raw figures used for analysis and raw data from the plots.

Research involving human participants, their data, or biological material

Policy information about studies with human participants or human data. See also policy information about sex, gender (identity/presentation), and sexual orientation and race, ethnicity and racism.

Reporting on sex and gender	-
Reporting on race, ethnicity, or other socially relevant groupings	-
Population characteristics	-
Recruitment	-
Ethics oversight	-

Note that full information on the approval of the study protocol must also be provided in the manuscript.

Field-specific reporting

Please select the one below that is the best fit for your research. If you are not sure, read the appropriate sections before making your selection.

☒ Life sciences ☐ Behavioural & social sciences ☐ Ecological, evolutionary & environmental sciences

For a reference copy of the document with all sections, see nature.com/documents/nr-reporting-summary-flat.pdf

Life sciences study design

All studies must disclose on these points even when the disclosure is negative.

Sample size	Given the complexity and the large variation between vesicles, data is not pooled together and only one GUVs is shown in text
Data exclusions	Only vesicles not showing active deformations were excluded.
Replication	Experiments were replicated in different days and conditions (. Vesicles in different conditions are also shown in Supporting Figure 1. Replication was successful. The conditions shown in text has been replicated three different times in two different days.
Randomization	No randomization was applied as each sample is different and contains different replicates.
Blinding	No blinding as observer bias does not play a role in this experiment.

Reporting for specific materials, systems and methods

We require information from authors about some types of materials, experimental systems and methods used in many studies. Here, indicate whether each material, system or method listed is relevant to your study. If you are not sure if a list item applies to your research, read the appropriate section before selecting a response.

Materials & experimental systems

n/a	Involved in the study
☒	☐ Antibodies
☒	☐ Eukaryotic cell lines
☒	☐ Palaeontology and archaeology
☒	☐ Animals and other organisms
☒	☐ Clinical data
☒	☐ Dual use research of concern
☒	☐ Plants

Methods

n/a	Involved in the study
☒	☐ ChIP-seq
☒	☐ Flow cytometry
☒	☐ MRI-based neuroimaging

Plants

Seed stocks	-
Novel plant genotypes	-
Authentication	-